Laboratory Investigation (2013) 93, 1054–1063

Subtraction micro-computed tomography of angiogenesis and osteogenesis during bone repair using synchrotron radiation with a novel contrast agent

Takeshi Matsumoto, Daichi Goto and Syota Sato

Quantitative three-dimensional (3D) imaging of angiogenesis during bone repair remains an experimental challenge. We developed a novel contrast agent containing 0.07- to 0.1-μm particles of zirconium dioxide (ZrCA) and established subtraction μCT using synchrotron radiation (sSRCT) for quantitative imaging of angiogenesis and bone repair. This method was applied to a rat model of tibial bone repair 3 days (DAY3; $n = 2$), 5 days (DAY5; $n = 8$), or 10 days (DAY10; $n = 8$) after drill-hole injury. Using the same drill-hole defect model, its potential use was illustrated by comparison of bone repair between hindlimbs subjected to mechanical unloading ($n = 6$) and normal weight bearing ($n = 6$) for 10 days. Following vascular casting with ZrCA, the defect site was scanned with 17.9- and 18.1-keV X-rays. In the latter, image contrast between ZrCA-filled vasculature and bone was enhanced owing to the sharp absorption jump of zirconium dioxide at 18.0 keV (k-edge). The two scan data sets were reconstructed with 2.74-μm voxel resolution, registered by mutual information, and digitally subtracted to extract the contrast-enhanced vascular image. K_2HPO_4 phantom solutions were scanned at 17.9 keV for quantitative evaluation of bone mineral. Angiogenesis had already started, but new bone formation was not found on DAY3. New bone emerged near the defect boundary on DAY5 and took the form of trabecular-like structure invaded by microvessels on DAY10. Vascular and bone volume fractions, blood vessel and bone thicknesses, and mineralization were higher on DAY10 than on DAY5. All these parameters were found to be decreased after 10 days of hindlimb unloading, indicating the possible involvement of angiogenesis in bone repair impairment caused by reduced mechanical stimuli. In conclusion, the combined technique of sSRCT and ZrCA vascular casting is suitable for quantitative 3D imaging of angiogenesis and its surrounding bone regeneration. This method will be useful for better understanding the linkage between angiogenesis and bone repair.
Laboratory Investigation (2013) **93,** 1054–1063; doi:10.1038/labinvest.2013.87; published online 8 July 2013

KEYWORDS: angiogenic microvasculature; bone defect regeneration; bone mineralization; k-edge absorption jump; monochromatic light; zirconium dioxide contrast agent

Vascular disruption accompanying bone fractures leads to the formation of hematoma, which recruits inflammatory and progenitor cells and provides an environment for these cells to secret cytokines and growth factors.[1,2] Among them, vascular endothelial growth factors are responsible for inducing angiogenesis in the early fracture hematoma.[3,4] Angiogenesis has a key role in bone repair by not only facilitating the supply of oxygen and nutrients required for bone repair and the removal of waste products but also by providing conduits for the invasion of osteoblast and osteoclast progenitors into the fracture site.[5,6] Thus, a lack of or inadequate angiogenesis significantly delays or compromises fracture healing.[7–9]

The involvement of angiogenesis in the outcome of bone repair is widely recognized but not entirely explored.[10] Increased understanding of the role of angiogenesis in bone repair is also crucial for designing new therapies, including the use of bone scaffold, for promoting bone fracture healing.[11–13] In this context, it is desirable to develop a quantitative imaging technique for structure analysis of neo-microvessels that proliferate through newly formed bone. High-resolution X-ray micro-computed tomography (μCT) combined with a vascular casting technique has been used for three-dimensional (3D) imaging of bone microvasculature in rodents.[14–18] In this technique, barium sulfate-gelatin or lead chromate-loaded silicon has been used as a vascular contrast-

Bioengineering Division, Osaka University Graduate School of Engineering Science, Toyonaka, Japan
Correspondence: Dr T Matsumoto, PhD, Bioengineering Division, Osaka University Graduate School of Engineering Science, 1-3 Machikaneyama-cho, Toyonaka 560-8531, Japan.
E-mail: matsu@me.es.osaka-u.ac.jp

Received 12 December 2012; revised 7 June 2013; accepted 11 June 2013

casting agent, and bone was often decalcified for extracting microvessels as the reconstructed absorption values in microvessels and bone do not differ much. Decalcification is disadvantageous for investigating the involvement of angiogenesis in bone repair.

Recently, it was demonstrated that μCT using synchrotron radiation provided good contrast between bone and barium-casted microvessels.[15,19,20] Monochromaticity of synchrotron light also allows measuring apparent mineralization,[21,22] serving as a metric of bone integrity. On the other hand, image registration and subtraction procedures for the two μCT scan sets of decalcified and undecalcified bone specimens containing a vascular contrast-casting agent have been proposed as a potential technique for precise image segmentation into vasculature and bone.[23] On the basis of referring to these techniques, we proposed that the sharp absorption jump at the X-ray energy (k-edge) specific to an appropriate vascular contrast-casting agent is available for quantitative imaging of angiogenesis and bone regeneration by subtraction μCT using synchrotron radiation (sSRCT). In this study, we developed a novel contrast agent containing zirconium dioxide particles (ZrCA) for vascular casting and established sSRCT for quantitative 3D imaging of angiogenesis and bone repair. Its feasibility was examined by application to early-stage defect repair in rat tibial cortical bone, where angiogenesis flourishes with bone regeneration. Furthermore, to illustrate its potential use, we investigated the involvement of angiogenesis in bone repair impairment in the defect of rat cortical bone under mechanical unloading.

MATERIALS AND METHODS

Contrast Agent Containing ZrCA for Vascular Casting

Agarose with a low-temperature melting point (Super LM; Nacalai Tesque, Kyoto, Japan) was dissolved in 0.1-M phosphate buffer solution (Nacalai Tesque, Kyoto, Japan) at a concentration of 1.2% w/v. The agarose solution was filtered sequentially using 47-mm disks of 8-, 3-, and 1.2-μm pore size (MF-Millipore; Millipore, Billerica, MA, USA) and stored at 40 °C in an incubator.

Just before use, ZrCA was prepared by mixing 30 ml of the agarose solution and 15 ml of zirconium dioxide hydrosol (ZR-40BL; Nissan Chemical Industries, Tokyo, Japan). The latter is a suspended solution of 0.07- to 0.1-μm particles of zirconium dioxide in water (62% w/v). These solutions were drawn separately into 50-ml syringes via 1.2-μm filters (Minisart; Sartorius, Gottingen, Germany) and mixed back and forth between the two syringes through a syringe junction $\geq$10 times in a 40 °C water bath. The viscosity of ZrCA ranged from 3.30 to 3.80 mPa s at shear rates of 38.3–689.4/s, measured at 40 °C with a cone-plate viscometer (TVE25L; Toki Sangyo, Tokyo, Japan), indicating the nearly Newtonian nature of this agent.

Animals

Experiments were conducted according to the guiding principles of the American Physiological Society and with the approval of the Animal Research Committee of Osaka University Graduate School of Engineering Science.

Preparation of Specimens at Different Stages of Bone Repair

Male Wistar rats aged 12 weeks (Clea Japan, Osaka, Japan) were anesthetized with intraperitoneal pentobarbital sodium (50 mg/kg). The skin over the medial aspect of the right lower leg was shaved, swabbed with povidone iodine, and incised. A full-thickness unicortical hole was created approximately 3 mm proximal to the tibio-fibula junction using a 0.9-mm diameter drill rotating at 11 000 RPM (Muromachi Kikai, Kyoto, Japan). Drill margins were frequently irrigated with saline to avoid thermal necrosis, and the drill hole was rinsed with a flushing syringe to discard bone fragments. After the arrest of bleeding from the bone marrow, the skin was sutured and swabbed again. The rats were single-housed with free access to standard food and water in standard conditions of temperature (25 $\pm$ 1 °C), humidity (60%), and light-controlled environment (12:12-h light–dark cycle). Buprenorphine (0.1 mg/kg) was administered subcutaneously *ad libitum* for pain relief.

The rats were similarly anesthetized again on postoperative days 3 (DAY3; $n=2$), 5 (DAY5; $n=8$), or 10 (DAY10; $n=8$). The abdominal wall was incised, and the aorta and vein were exposed by blunt dissection. The rat was warmed with an infrared heater (HIR-227; Omron, Kyoto, Japan), and the gut was moistened with warmed saline as needed. Following intravenous heparin (1000 U), both vessels were ligated distal to the renal branches. Following this, the aorta was cannulated with a polyethylene catheter in the distal direction, and the vein was incised at the femoral junction to permit the elution of blood and the infused solutions. The lower body was flushed with 50 ml of heparinized saline (37 °C, 100 U/ml) and subsequently with 5 ml of 0.1-M phosphate buffer solution (37 °C), which is required for avoiding an adverse effect of saline on ZrCA. ZrCA (40 °C) was then perfused from a reservoir with a head pressure of 120 mm Hg. The rat was euthanized by pentobarbital sodium overdose. The defect-side hindlimb was moved occasionally by hand to facilitate extensive perfusion. Upon completion of perfusion, the femoral artery and vein in the defect side were ligated, and the whole body was immersed into an ice-cold water bath for $\sim$1 h and stored overnight at 4 °C. The drill-holed tibia was then harvested and soaked in 70% ethanol at 4 °C for 7 days. The defect segment was cut out with a low-speed diamond wheel saw (SBT650; South Bay Technology, San Clemente, CA, USA) and sealed into a polyethylene tube containing ethanol.

Preparation of Specimens Subjected to Mechanical Unloading

Female Fischer rats aged 12 weeks (Clea Japan, Osaka, Japan) were operated on with a 0.7-mm drill hole on a tibial diaphysis with a similar procedure as described above and either subjected to hindlimb unloading through a tail suspension

procedure ($n=6$) or kept unsuspended ($n=6$) for 10 days. The tail-suspension procedure was performed according to the recommendations of Morey-Holton and Globus.[24] Tail-suspended rats were permitted 360° of movement around the cage using their forelimbs while their hindlimbs were kept free of bearing weight. The suspension height was adjusted to prevent the hindlimbs from touching any supportive surface, with care taken to maintain a head-down tilt angle below 30°. Each tail-suspended and weight-bearing control rat was kept individually and underwent the protocol of ZrCA vascular casting on postoperative day 10, and the drill-holed tibial specimens were obtained in the above-mentioned manner.

Synchrotron Radiation CT

We used a high-resolution CT system installed in the beamline 20B2 of the synchrotron radiation facility SPring-8 (Harima, Japan). The bone specimen was mounted on a stack of computer-controlled precision stages. The photon flux transmitted through the specimen was transformed into visible light through a 10-μm-thick phosphor screen ($Gd_2O_2S:Tb^+$) and detected by a high-resolution detector consisting of a beam monitor (AA40P; Hamamatsu Photonics, Hamamatsu, Japan) and a cooled CCD camera (C4880-41 S; Hamamatsu Photonics). Images of the specimen and the X-ray beam alone were acquired with 1-s exposure per frame over an angular range of 0°–180° in 0.2° and 1° steps, respectively. The latter was used for calibration to compensate for X-ray source instability. For background correction, 10 images of CCD dark current were acquired at the start and end of the scan. Reconstruction was made with a two-dimensional filtered backward projection algorithm, providing contiguous two-dimensional images composed of 2.74-μm cubic voxels with 16-bit resolution.

The sample was scanned just above (18.1 keV) and below (17.9 keV) the zirconium dioxide k-edge energy. Reconstructed images were redigitized with 8-bit gray-scale resolution such that voxel values of the linear absorption coefficient, μ (/cm), were given by $0.392 \times$ gray value (0(black)–255(white)), yielding a pair of normalized 18.1- and 17.9-keV image stacks with the gray value ranging from 0 to 255 and from 0 to $\sim$60, respectively. A pair of such normalized 17.9- and 18.1-keV images was used for image segmentation as described later.

For quantitative evaluation of mineralization, capillary tubes containing K_2HPO_4 water solution at various concentrations (0.38–1.30 g/cm^3), serving as hydroxyapatite phantoms,[21,22] were also scanned at 17.9 keV in the same manner as the specimen imaging. Phantom images were redigitized such that μ was given by $0.0588 \times$ gray value, leading the relationship between the density of hydroxyapatite, d.HAp (g/cm^3), and gray value: $\text{d.HAp} = 0.136 \times \mu - 0.142 = 7.97 \times 10^{-3} \times \text{gray value} - 0.142$ ($r^2 > 0.999$). This relation was applied to 17.9-keV bone images redigitized similarly as for the phantom images. Note that the quantification of bone mineralization here assumed that bone tissue was uniform and that its absorption could be represented by a two-phase mixture of hydroxyapatite and other light elements, replaced by K_2HPO_4 and water, respectively. Thus, d.HAp is only the measure of apparent mineralization.

Image Segmentation by Subtraction

The sharp change in μ of zirconium dioxide at its k-edge yields local differences of image intensity between 17.9- and 18.1-keV images, thereby highlighting vascular structures. Before image subtraction for vascular extraction, a pair of normalized 17.9- and 18.1-keV image stacks was first corrected for any misalignment, which was mainly attributed to the return-to-origin error of the rotational specimen stage. An image-registration technique based on mutual information was used for matching the two image stacks.[25]

Even with the fine alignment, however, unwanted residuals near bone boundaries remained owing to partial-volume effects attributed to the limited resolution. Unfortunately, some of these residuals were comparable in image intensity to those indicating microvessels, thus their removal from the residual image stack was not straightforward. To reduce this artifactual error, grayscale dilation (ie, 3D maximum filtering) was applied to the 17.9-keV image stack before subtraction, which replaced each voxel with the nearby voxel of the highest gray value, leading to an expansion of the bone region. The residual image stack was then obtained by subtracting the modified 17.9-keV image stack from the original 18.1-keV one, and following $3 \times 3 \times 3$ voxel averaging, every voxel with an image intensity higher than the maximum intensity in the region outside the specimen was included among the vascular region. The original 17.9-keV image stack was then filtered by $3 \times 3 \times 3$ voxel averaging, and all regions $\geq$4.74/cm (d.HAp $\geq$0.5 g/cm^3) other than vasculature were classified as regenerated bone.

To evaluate the validity of sSRCT for extracting angiogenic vessels from the defect region, a comparison was made between the reconstructed image and the light micrograph of a cortical transverse section for one specimen on DAY10. The microscopic section was obtained after CT scanning by embedding a specimen in methylmethacrylate and grinding it to a thickness of 30 μm, followed by toluidine blue staining. The reconstructed image stack comprising 11 2.74-μm-thick slices (ie, nearly 30-μm thick) was matched to the micrograph using the above-mentioned image-registration technique. The light micrograph was resampled to the same resolution as the SRCT image (2.74 μm) before matching.

Quantitative Parameters for Vascular and Bone Structures

For structural analysis (excluding DAY3 specimens), a cylindrical region of interest was chosen within the cortical defect. Newly formed bone along the inner edge of the defect boundary and an extensive accumulation of ZrCA, which was found exclusively near the periosteal surface on some

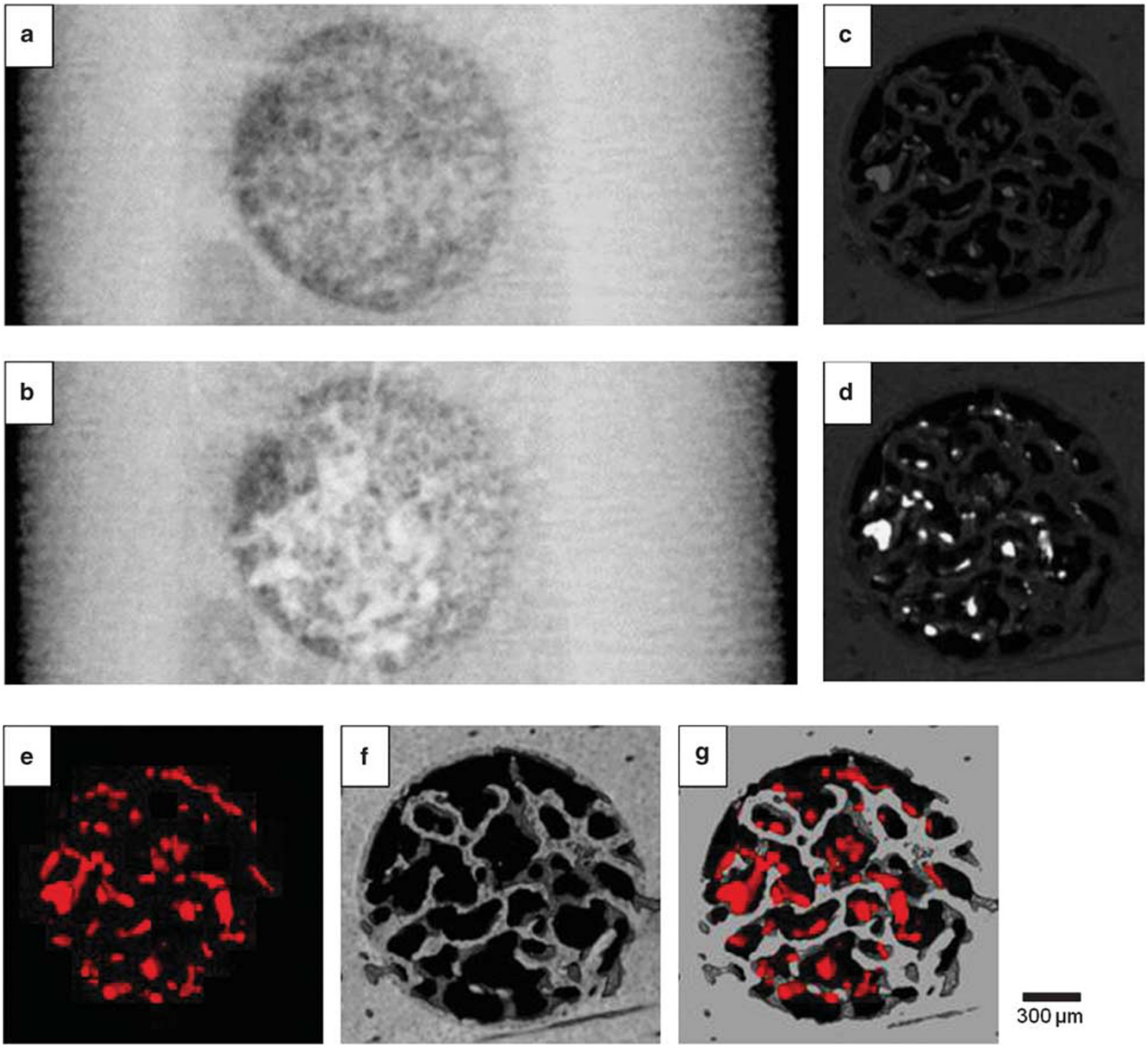

Figure 1 Bone defect images in a tibial diaphysis 10 days after drill-hole injury. (**a**, **b**) X-ray transmission images at 17.9 keV (**a**) and 18.1 keV (**b**). (**c**, **d**) Image stacks reconstructed from scan data sets at 17.9 keV (**c**) and 18.1 keV (**d**), comprising 20 2.74-μm-thick slices perpendicular to the drill-hole direction. The enhanced contrast between angiogenic vessels and bone on 18.1-keV images is due to the sharp absorption jump of ZrCA at the energy just above its k-edge. (**e**–**g**) Image stacks of blood vessels (**e**), bone (**f**), and their fusion (**g**), produced from the images of **c** and **d** through the image registration and subtraction procedures. Bone regions are >80 on a 0–255 gray scale, corresponding to the apparent mineral density of >0.5 g/cm^3. In (**f**), voxel values of gray scale are proportional to measures of mineralization. All images are displayed at the same magnification.

specimens on DAY5, were not included in the region of interest. Volume fraction of vasculature, V.Vf (%), mean thickness of blood vessels, V.Th (μm), volume fraction of bone, B.Vf (%), and mean thickness of bone, B.Th (μm), were calculated. The BoneJ plugin 1.3.5 for ImageJ 1.46k[26] was used for determining all indexes. The frequency distribution of d.HAp and its mean and median values were also determined using the μ-d.HAp relation.

Statistics

Data are presented as mean ± s.e. Differences between DAY5 and DAY10, and between the control and unloaded rats, were assessed by the two-tailed Mann–Whitney *U*-test using Prism 4 (version 4.0c; GraphPad Software, San Diego, CA, USA). A value of $P<0.05$ was considered statistically significant.

RESULTS

Images of a tibial defect on DAY10 are shown in Figure 1. Contrast enhancement of angiogenic vessels owing to the absorption jump of ZrCA is evident in both transmission images at 17.9 keV (Figure 1a) and 18.1 keV (Figure 1b) and reconstructed image stacks at 17.9 keV (Figure 1c) and 18.1 keV (Figure 1d). Image contrast between angiogenic vessels and bone was enhanced at 18.1 keV, while bone

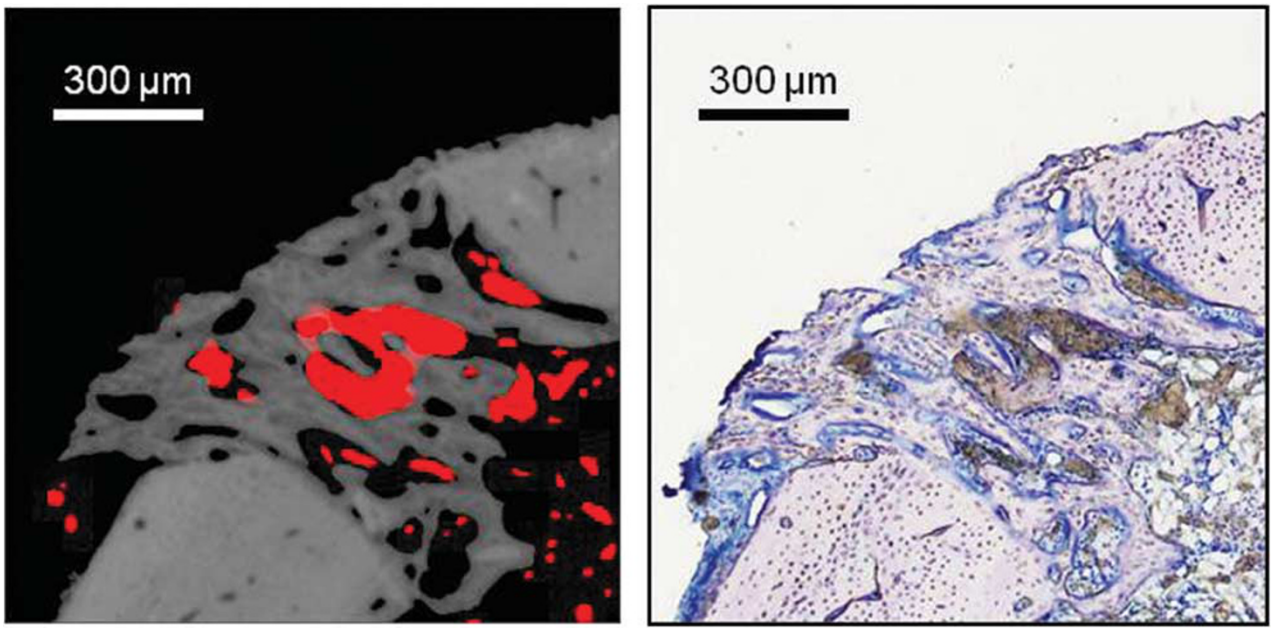

Figure 2 Comparison between a light micrograph and a reconstructed image of a tibial defect 10 days after drill-hole injury. Right: Undecalcified 30-μm-thick section stained with toluidine blue. Mineralized bone is light purple; non-mineralized bone (osteoid tissue) is blue. ZrCA-filled blood vessels are brownish-red. Left: Volume-rendered display of blood vessels (red) and bone (gray), comprising 11 2.74-μm-thick reconstructed slices matched to the micrograph by image registration.

regions showed virtually the same gray level in both 17.9- and 18.1-keV images, allowing image segmentation into vasculature and bone. Blood vessels were extracted (Figure 1e) by image subtraction between Figures 1c and d. The extra-vascular space was segmented into bone and background with a threshold of d.HAp $= 0.5\,g/cm^3$ (Figure 1f), where gray values in bone regions were redigitized such that d.HAp (g/cm^3) was given by $7.97 \times 10^{-3} \times$ gray value $- 0.142$. This bone image was binarized and combined with Figure 1e to yield the fusion image (Figure 1g).

In Figure 2, the light micrograph of a defect transverse section stained with toluidine blue was compared with the reconstructed image, which was closely matched with the micrograph and segmented into blood vessels (red) and bone (gray). Blood vessels filled with ZrCA (brownish-red) as well as bone were generally well reproduced in the volume-rendered image, and the efficacy of histology with ZrCA infusion was indicated.

Figure 3a shows 18.1-keV transmission images of cortical defects on DAY3, DAY5, and DAY10 and 3D displays of vasculature and bone within each defect. Angiogenesis developed ahead of bone formation; only blood vessels with an irregular shape were observed on DAY3. Bone seems to be formed sparsely in a tree-like manner inward from the defect boundary on DAY5 and expanded widely throughout the defect with formation of trabecular-like structures on DAY10. The plots of V.Vf *vs* B.Vf and V.Th *vs* B.Th on DAY5 ($n = 8$) and DAY10 ($n = 8$) are shown in Figures 3b and c, respectively. All measures were significantly higher on DAY10 than on DAY5: V.Vf and B.Vf were $5.4 \pm 1.5\%$ and $4.3 \pm 1.3\%$ on DAY5, and $14.4 \pm 3.0\%$ and $30.6 \pm 1.4\%$ on DAY10, respectively; V.Th and B.Th were 31.2 ± 2.0 and $10.7 \pm 0.4\,\mu$m on DAY5 and 43.6 ± 3.0 and $26.0 \pm 0.9\,\mu$m on DAY10, respectively. Figure 3d compares the relative distributions of d.HAp within the defect on DAY5 and DAY10. Mean/median values for the distribution were both higher on DAY10 than on DAY5 ($1.03 \pm 0.01/1.06 \pm 0.01$ *vs* $0.72 \pm 0.01/0.74 \pm 0.01\,g/cm^3$; $P < 0.005$). All these values were $< 1.36 \pm 0.02/1.38 \pm 0.02\,g/cm^3$ around the outside of the defect on DAY10 ($P < 0.001$).

Figure 4 shows portions of the defect-hole circumference on DAY5 and DAY10. Newly formed bone appeared in fragments away from the defect boundary or in a tree-like manner in contact with the intact bone on DAY5. Mineral apposition along the inner hole-edge, which was almost undetectable on DAY5, was observed on DAY10.

Mechanical unloading impaired the defect repair as shown in representative 3D displays in Figure 5a. In unloaded rats, blood vessels and bone were less developed and not formed yet in the central portion of the defect; furthermore, mineralization was less evident. The plots of V.Vf *vs* B.Vf and V.Th *vs* B.Th show that all these measures were significantly reduced by unloading (Figures 5b and c); V.Vf, B.Vf, V.Th, and B.Th were $4.3 \pm 0.6\%$, $26.3 \pm 3.3\%$, $26.8 \pm 0.5\,\mu$m, and $21.7 \pm 1.7\,\mu$m in hindlimb-unloaded rats ($n = 6$); these were significantly smaller than $8.1 \pm 1.2\%$, $45.4 \pm 2.6\%$, $32.4 \pm 0.6\,\mu$m, and $34.2 \pm 1.7\,\mu$m, respectively, in control rats ($n = 6$). Figure 5d compares the relative distributions of

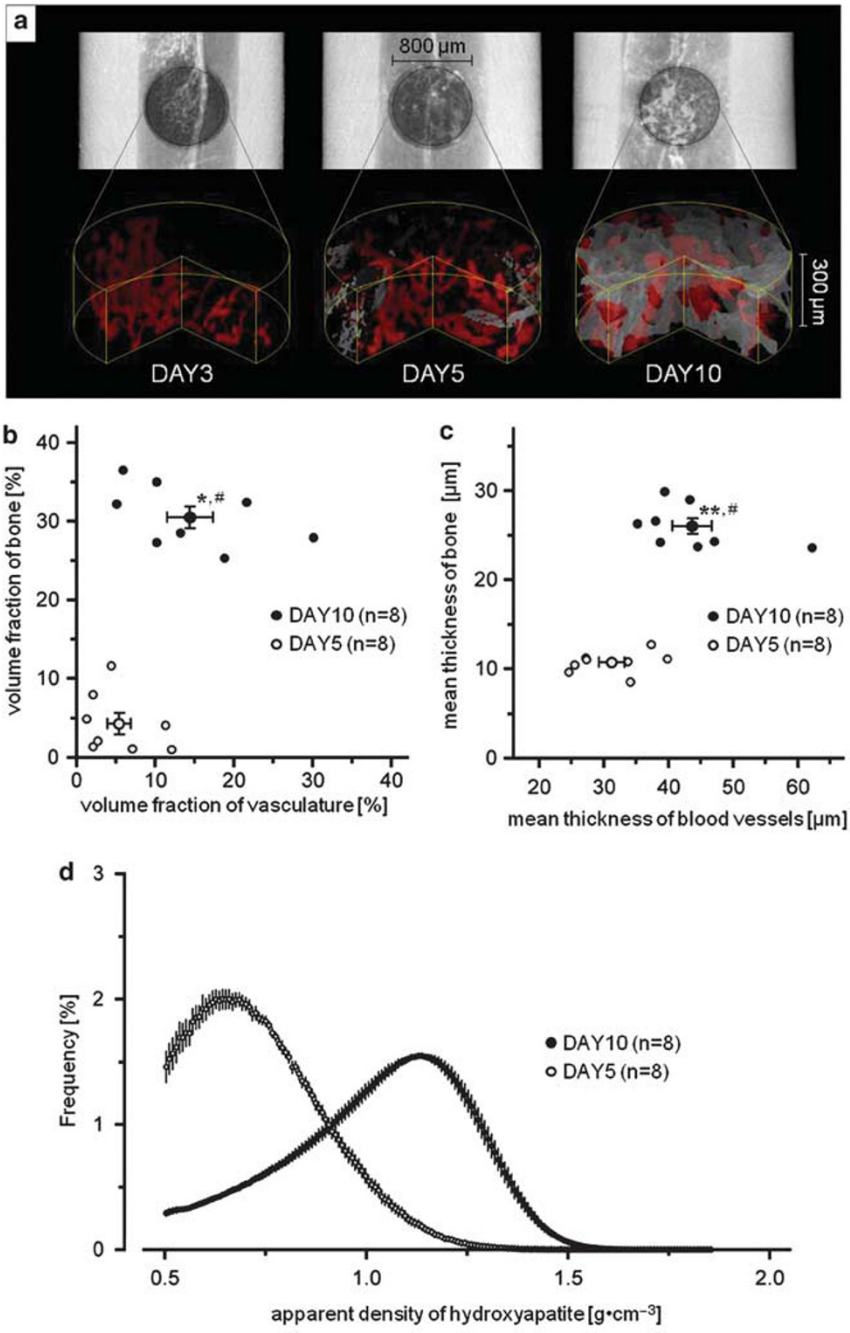

Figure 3 Angiogenesis and bone formation in a tibial defect 3 (DAY3), 5 (DAY5), and 10 (DAY10) days after drill-hole injury. (**a**) Transmission images at 18.1 keV and volume-rendered displays of blood vessels (red) and bone (gray). (**b**) Plots of volume fractions of vasculature (V.Vf) *vs* bone (B.Vf) in each defect on DAY5 and DAY10 and their respective means ± s.e. $^{*}P<0.05$ *vs* V.Vf on DAY5; $^{\#}P<0.001$ *vs* B.Vf on DAY5. (**c**) Plots of thicknesses of blood vessels (V.Th) *vs* bone (B.Th) in each defect on DAY5 and DAY10 and their respective means ± s.e. $^{**}P<0.005$ *vs* V.Th on DAY5; $^{\#}P<0.001$ *vs* B.Th on DAY5. (**d**) Distributions of relative voxel frequency *vs* density of hydroxyapatite (d.HAp) in the defect on DAY5 and DAY10. Values of mean ± s.e. were determined by normalizing the voxel frequencies counted in each d.HAp (bin width = 8 mg/cm^3) to the total number of voxels with d.HAp of >0.5 g/cm^3 for each defect.

d.HAp with and without unloading. There was an appreciable delay of mineralization in hindlimb-unloaded rats. Mean/median values for the distribution were both lower in hindlimb-unloaded than in control rats (0.73 ± 0.02/0.70 ± 0.03 *vs* 0.93 ± 0.02/0.95 ± 0.02 g/cm^3; $P<0.005$).

DISCUSSION

We developed a novel vascular contrast-casting agent (ZrCA) for sSRCT and imaged angiogenesis and bone regeneration, and also assessed mineralization, in rat tibial drill-hole defects at early healing stages. The sharp contrast change owing

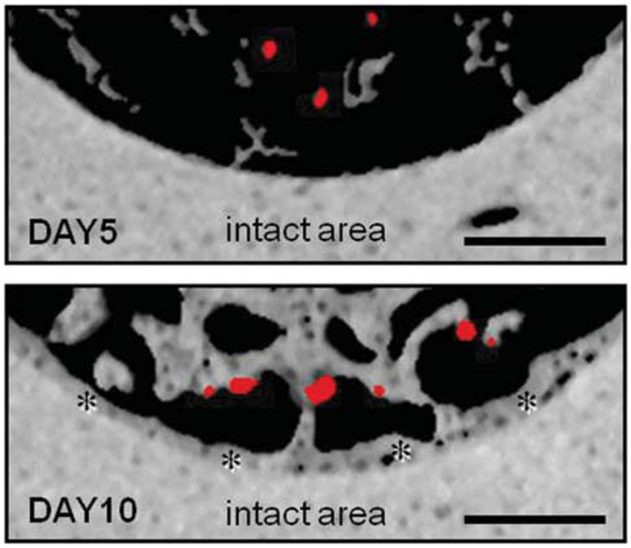

Figure 4 Reconstructed images of vasculature and bone near the boundary of the cortical defect 5 (DAY5) and 10 (DAY10) days after drill-hole injury. Bone mineral apposition (*) is evident along the inner edge of the defect on DAY10. Voxel values of gray scale are proportional to measures of mineralization. Bar = 150 μm.

to the zirconium dioxide k-edge allowed the clear segmentation of microvasculature and bone for quantitative evaluation of their structures and bone mineralization in the course of the repair process. Furthermore, this method could quantify the deleterious effect of mechanical unloading on early-stage bone repair, showing its potential as a valuable tool for angiogenesis-coupled bone-healing research. To our knowledge, this is the first application of sSRCT that takes advantage of the absorption jump at the k-edge to the observational study of angiogenesis in conjunction with bone regeneration.

Barium sulfate-gelatin or radiopaque silicon polymer has been commonly used as vascular contrast-casting agents in μCT imaging of small animal vasculatures. However, these agents might not produce sufficient image contrast between vasculature and bone, and it was very often the case that bone was decalcified to identify vasculature from surrounding bone. Increasing the content of contrast materials will be effective for enhancing the image contrast but detrimental to vascular perfusability. On the other hand, taking advantage of the high light intensity, practically no beam-hardening artifacts, and a high signal-to-noise ratio, synchrotron radiation μCT allows for the quantitative 3D assessment of vascular and bone structures with commonly used contrast agents.[15,19,20] However, contrast enhancement of vasculature could be uneven, especially in non-tree-like microvascular beds, owing to incomplete perfusion as well as inhomogeneous dispersion, settling, or clumping of contrast materials during infusion.[27] Given that vascular image intensity is spatially heterogeneous and not so very different locally from bone image intensity, segmentation into microvasculature and bone is not straightforward even by synchrotron radiation μCT.

Images acquired above and below the k-edge of a material allow a simple subtraction algorithm to retrieve its structure while removing practically all other structures and background. The high detection sensitivity and quantitative performance of this type of imaging have been reported in angiography and lung imaging using iodine and xenon, respectively, as contrast agents.[28,29] Here, we focused on the zirconium dioxide k-edge that is close to the energy suitable for μCT imaging of rodent cortical bone[22,30] and developed ZrCA for sSRCT, which provides several advantages in bone microvascular imaging.

Angiogenic vessels are likely to be destabilized for remodeling or degradation; thus, these vessels are immature, leaky, and vulnerable to rupture.[31] Therefore, perfusion pressure for vascular casting in bone defects during early-stage healing should not elevate beyond physiological levels. With the use of agarose, the viscosity of ZrCA is similar to the apparent blood viscosity in microvasculature, which has been reported to be <5 mPa s at 37 °C,[32] thereby allowing the use of ZrCA under a physiological perfusion pressure. Indeed, a similarly low-concentrated agarose solution containing barium or fluorescent microbeads showed easy vascular perfusability in earlier studies.[33,34] Furthermore, the hydrophilicity of ZrCA could contribute to militating for its vascular penetration. That is, ZrCA can be easily miscible with the pre-perfused buffer solution, thereby reducing a possibility of patchy perfusion[16] in a non-tree-like vascular network, where diffusion, rather than convection, may be the primary transport mechanism in some vessels.

To facilitate the capability of sSRCT for quantitative bone imaging, the intensity of the X-ray should also yield appropriate overall attenuation through the specimen at the zirconium dioxide k-edge. For rat tibial bone imaging at SPring-8, the 20-keV X-ray yielded good contrast with a high signal-to-noise ratio, allowing quantitative evaluation of its cortical microstructure and mineralization.[22,30] The zirconium dioxide k-edge (18 keV) is not far from 20 keV, and the light brilliance is as extremely high at 18 keV as at 20 keV in SPring-8 (http://www.spring8.or.jp/en/about_us/whats_sr/sp8_features/). Thus, the X-ray energy close to 18 keV is ideal for not only separately imaging of vascular and bone microstructures of small or rodent bone specimen but also assessment of its mineral density, which shows region-to-region and time-to-time variations during bone repair.[35]

This method enabled the quantification of angiogenesis and bone regeneration during the early-stage drill-hole defect healing and showed rapid vascular and bone formation. In addition, it revealed a tree-like bone ingrowth from the defect edge where new bone subsequently accumulated. In the present rat model of bone repair, the small drill hole was created at a mechanically stable site,[36] and normal gait activity started soon after the defect production. Consequently, daily or physiological mechanical stimuli,

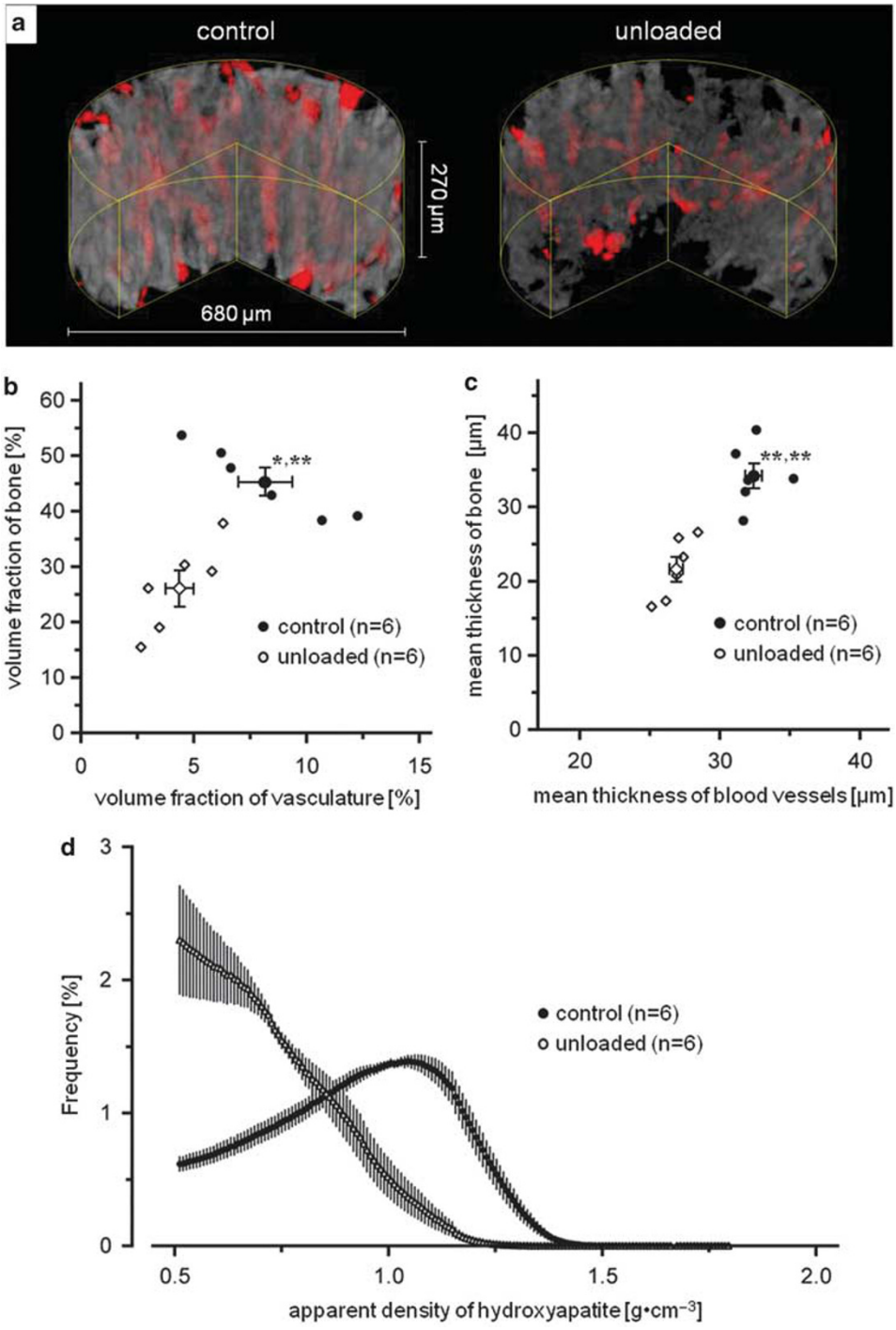

Figure 5 Deleterious effect of mechanical unloading on angiogenesis and bone regeneration 10 days after drill-hole injury. (**a**) Volume-rendered displays of blood vessels (red) and bone (gray) in a drill-hole defect of control (left) and hindlimb-unloaded (right) rats. Bone regions with darker gray are mineralized to the lower degree. (**b**) Plots of volume fractions of vasculature (V.Vf) *vs* bone (B.Vf) in each defect for control and hindlimb-unloaded rats and their respective means ± s.e. $*P<0.05$ *vs* control V.Vf; $**P<0.005$ *vs* control B.Vf. (**c**) Plots of thicknesses of blood vessels (V.Th) *vs* bone (B.Th) in each defect for control and hindlimb-unloaded rats and their respective means ± s.e. $**P<0.005$ *vs* control V.Th or B.Th. (**d**) Distributions of relative voxel frequency *vs* density of hydroxyapatite (d.HAp) in the defect of control and hindlimb-unloaded rats, shown in the same manner as in Figure 3d.

which will serve in enhancing osteogenesis and hypoxia-mediated angiogenesis,[37–39] were induced from the very early stage of bone repair. Angiogenesis encourages bone regeneration by contributing to both the sustainment of the high metabolic activity of osteoblasts engaged in bone repair and the recruitment of osteoprogenitors to the defect

zone.[5,40] Thus, the bone repair process that occurred in the present defect model may be somewhat facilitated according to such a specific mechanical environment. Indeed, in the same rat model of bone repair, hindlimb unloading reduced vascular ingrowth and impaired bone repair in terms of both volume and mineralization.

The results could demonstrate the potential of sSRCT combined with ZrCA vascular casting in exploring the bone repair process on the basis of 3D imaging of bone regeneration and its requisite angiogenesis. Vascular casting with ZrCA may also be compatible with section preparation for conventional bone stainings, thereby permitting histological evaluation complementary to the present image quantification. However, fracture healing occurs under a variety of biological and biomechanical environments[41–43] and, in most clinical cases, goes through a mixed process of intramembranous and endochondral bone formation. Endochondral ossification is the process of bone formation arising from a pre-existing cartilage framework while in intramembranous ossification, the bone arises *de novo* without the benefit of an underlying cartilage skeleton. In the rodent drill-hole defect model, however, intramembranous ossification is likely dominant.[17,44] Thus, the feasibility of the present technique in conjunction with histological procedures should be confirmed in bone fractures with variable patterns of distraction and mechanical instability that will generate complexly intertwined vascular and bone structures compared with those presently observed.

Aside from the above issue, there are several limitations for this method. Even with higher resolution and signal-to-noise ratio than those of standard μCT, the limited voxel resolution may cause apparent discontinuities in some newly formed vascular and bone segments with less than several micrometer thickness. The fragility of agarose gel also increases the possibility of causing disjointed vascular network images. Furthermore, although the extravasation of ZrCA would be less likely to occur owing to the use of physiological perfusion pressure (120 mm Hg) for vascular casting, the possibility could not been ruled out. It will be difficult to identify the extravasated ZrCA among angiogenic vessels, if any, particularly when it occurs on a scale similar to or smaller than the size of microvessels. Advanced high-resolution imaging modalities and rule-based segmentation algorithms[45,46] are required to boost the performance of sSRCT. Finally, it should be noted that because the available energy of X-rays is limited to near the zirconium dioxide k-edge, this method would be unsuitable for specimens that need high-energy X-rays far beyond the zirconium dioxide k-edge, including a thick wall of dense compact bone and bone-implant interfaces.[19,20,47]

In conclusion, we have established the feasibility of the combined technique of sSRCT and ZrCA vascular casting in quantitative 3D imaging of angiogenesis and bone repair. Its application to early-stage bone repair in rat cortical drill-hole defects could quantify the impact of mechanical stimuli on vascular ingrowth and bone repair, demonstrating the potential of the present imaging method for the enhanced understanding of angiogenesis and its involvement in bone repair.

ACKNOWLEDGEMENTS

The sSRCT experiments were performed at SPring-8 with the approval of the Japan Synchrotron Radiation Research Institute (proposal no. 2008A1078 and no. 2008B1512). Part of this work was supported by a Grant-in-Aid for Scientific Research from the Ministry of Education, Culture, Sports, Science and Technology of the Japanese government (20300158).

DISCLOSURE/CONFLICT OF INTEREST

The authors declare no conflict of interest.

1. Oe K, Miwa M, Sakai Y, *et al.* An *in vitro* study demonstrating that haematomas found at the site of human fractures contain progenitor cells with multilineage capacity. J Bone Joint Surg Br 2007;89:133–138.
2. Schindeler A, McDonald MM, Bokko P, *et al.* Bone remodeling during fracture repair: the cellular picture. Semin Cell Dev Biol 2008;19:459–466.
3. Street J, Winter D, Wang JH, *et al.* Is human fracture hematoma inherently angiogenic? Clin Orthop Relat Res 2000;378:224–237.
4. Carano RA, Filvaroff EH. Angiogenesis and bone repair. Drug Discov Today 2003;8:980–989.
5. Maes C, Kobayashi T, Selig MK, *et al.* Osteoblast precursors, but not mature osteoblasts, move into developing and fractured bones along with invading blood vessels. Dev Cell 2010;19:329–344.
6. Kindle L, Rothe L, Kriss M, *et al.* Human microvascular endothelial cell activation by IL-1 and TNF-alpha stimulates the adhesion and transendothelial migration of circulating human CD14+ monocytes that develop with RANKL into functional osteoclasts. J Bone Miner Res 2006;21:193–206.
7. Fang TD, Salim A, Xia W, *et al.* Angiogenesis is required for successful bone induction during distraction osteogenesis. J Bone Miner Res 2005;20:1114–1124.
8. Hausman MR, Schaffler MB, Majeska RJ. Prevention of fracture healing in rats by an inhibitor of angiogenesis. Bone 2001;29:560–564.
9. Street J, Bao M, deGuzman L, *et al.* Vascular endothelial growth factor stimulates bone repair by promoting angiogenesis and bone turnover. Proc Natl Acad Sci USA 2002;99:9656–9661.
10. Keramaris NC, Calori GM, Nikolaou VS, *et al.* Fracture vascularity and bone healing: a systematic review of the role of VEGF. Injury 2008;39(Suppl 2):S45–S57.
11. Hankenson KD, Dishowitz M, Gray C, *et al.* Angiogenesis in bone regeneration. Injury 2011;42:556–561.
12. Wan C, Gilbert SR, Wang Y, *et al.* Activation of the hypoxia-inducible factor-1alpha pathway accelerates bone regeneration. Proc Natl Acad Sci USA 2008;105:686–691.
13. Kanczler JM, Oreffo RO. Osteogenesis and angiogenesis: the potential for engineering bone. Eur Cell Mater 2008;15:100–114.
14. Moore DC, Leblanc CW, Müller R, *et al.* Physiologic weight-bearing increases new vessel formation during distraction osteogenesis: a micro-tomographic imaging study. J Orthop Res 2003;21:489–496.
15. Schneider P, Krucker T, Meyer E, *et al.* Simultaneous 3D visualization and quantification of murine bone and bone vasculature using micro-computed tomography and vascular replica. Microsc Res Tech 2009;72:690–701.
16. Sider KL, Song J, Davies JE. A new bone vascular perfusion compound for the simultaneous analysis of bone and vasculature. Microsc Res Tech 2010;73:665–672.
17. He YX, Zhang G, Pan XH, *et al.* Impaired bone healing pattern in mice with ovariectomy-induced osteoporosis: a drill-hole defect model. Bone 2011;48:1388–1400.
18. Nyangoga H, Mercier P, Libouban H, *et al.* Three-dimensional characterization of the vascular bed in bone metastasis of the rat by microcomputed tomography (MicroCT). PLoS One 2011;6:e17336.

19. Fei J, Peyrin F, Malaval L, *et al.* Imaging and quantitative assessment of long bone vascularization in the adult rat using microcomputed tomography. Anat Rec (Hoboken) 2010;293:215–224.
20. Roche B, David V, Vanden-Bossche A, *et al.* Structure and quantification of microvascularisation within mouse long bones: what and how should we measure? Bone 2012;50:390–399.
21. Nuzzo S, Peyrin F, Cloetens P, *et al.* Quantification of the degree of mineralization of bone in three dimensions using synchrotron radiation microtomography. Med Phys 2002;29:2672–2681.
22. Matsumoto T, Yoshino M, Asano T, *et al.* Monochromatic synchrotron radiation μCT reveals disuse-mediated canal network rarefaction in cortical bone of growing rat tibiae. J Appl Physiol 2006;100: 274–280.
23. Morgan EF, Hussein AI, Al-Awadhi BA, *et al.* Vascular development during distraction osteogenesis proceeds by sequential intramuscular arteriogenesis followed by intraosteal angiogenesis. Bone 2012;51: 535–545.
24. Morey-Holton ER, Globus RK. Hindlimb unloading rodent model: technical aspects. J Appl Physiol 2002;92:1367–1377.
25. Maes F, Collignon A, Vandermeulen D, *et al.* Multimodality image registration by maximization of mutual information. IEEE T Med Imaging 1997;16:187–198.
26. Doube M, Kłosowski MM, Arganda-Carreras I, *et al.* BoneJ: free and extensible bone image analysis in ImageJ. Bone 2010;47:1076–1079.
27. Marxen M, Thornton MM, Chiarot CB, *et al.* MicroCT scanner performance and considerations for vascular specimen imaging. Med Phys 2004;31:305–313.
28. Dilmanian FA. Computed tomography with monochromatic x rays. Am J Physiol Imaging 1992;7:175–193.
29. Suortti P, Thomlinson W. Medical applications of synchrotron radiation. Phys Med Biol 2003;48:R1–35.
30. Matsumoto T, Ando N, Tomii T, *et al.* Three-dimensional cortical bone microstructure in a rat model of hypoxia-induced growth retardation. Calcif Tissue Int 2011;88:54–62.
31. Jussila L, Alitalo K. Vascular growth factors and lymphangiogenesis. Physiol Rev 2002;82:673–700.
32. Fung Y. Biomechanics: Mechanical Properties of Living Tissues, London, UK, 1990.
33. Barou O, Mekraldi S, Vico L, *et al.* Relationships between trabecular bone remodeling and bone vascularization: a quantitative study. Bone 2002;30:604–612.
34. Dutly AE, Kugathasan L, Trogadis JE, *et al.* Fluorescent microangiography (FMA): an improved tool to visualize the pulmonary microvasculature. Lab Invest 2006;86:409–416.
35. Manjubala I, Liu Y, Epari DR, *et al.* Spatial and temporal variations of mechanical properties and mineral content of the external callus during bone healing. Bone 2009;45:185–192.
36. Prasad J, Wiater BP, Nork SE, *et al.* Characterizing gait induced normal strains in a murine tibia cortical bone defect model. J Biomech 2010;43:2765–2770.
37. Wohl GR, Towler DA, Silva MJ. Stress fracture healing: fatigue loading of the rat ulna induces upregulation in expression of osteogenic and angiogenic genes that mimic the intramembranous portion of fracture repair. Bone 2009;44:320–330.
38. Groothuis A, Duda GN, Wilson CJ, *et al.* Mechanical stimulation of the pro-angiogenic capacity of human fracture haematoma: involvement of VEGF mechano-regulation. Bone 2010;47:438–444.
39. Boerckel JD, Uhrig BA, Willett NJ, *et al.* Mechanical regulation of vascular growth and tissue regeneration *in vivo*. Proc Natl Acad Sci USA 2011;108:E674–E680.
40. Colnot C. Skeletal cell fate decisions within periosteum and bone marrow during bone regeneration. J Bone Miner Res 2009;24:274–282.
41. Utvåg SE, Grundnes O, Reikerås O. Effects of lesion between bone, periosteum and muscle on fracture healing in rats. Acta Orthop Scand 1998;69:177–180.
42. Marsh DR, Li G. The biology of fracture healing: optimising outcome. Br Med Bull 1999;55:856–869.
43. Augat P, Simon U, Liedert A, *et al.* Mechanics and mechano-biology of fracture healing in normal and osteoporotic bone. Osteoporos Int 2005;16(Suppl 2):S36–4.
44. Monfoulet L, Rabier B, Chassande O, *et al.* Drilled hole defects in mouse femur as models of intramembranous cortical and cancellous bone regeneration. Calcif Tissue Int 2010;86:72–81.
45. Waarsing JH, Day JS, Weinans H. An improved segmentation method for *in vivo* microCT imaging. J Bone Miner Res 2004;19:1640–1650.
46. Foruzan AH, Zoroofi RA, Sato Y, *et al.* Hessian-based filter for vascular segmentation of noisy hepatic CT scans. Int J Comput Assist Radiol Surg 2012;7:199–205.
47. Stadlinger B, Pilling E, Mai R, *et al.* Effect of biological implant surface coatings on bone formation, applying collagen, proteoglycans, glycosaminoglycans and growth factors. J Mater Sci Mater Med 2008; 19:1043–1049.